Journal of Electromagnetic Waves and Applications

ISSN: 0920-5071 (Print) 1569-3937 (Online) Journal homepage: www.tandfonline.com/journals/tewa20

Multi-resonator plasmonic metasurface biosensor with graphene enhancement for ultra-sensitive terahertz pregnancy detection using machine learning optimization

Jacob Wekalao, Jonas Muheki, Hussein A. Elsayed, Ahmed Mehaney, Sarah I. Othman, Mostafa R. Abukhadra, Stefano Bellucci, Amuthakkannan Rajakannu & William Ochen

To cite this article: Jacob Wekalao, Jonas Muheki, Hussein A. Elsayed, Ahmed Mehaney, Sarah I. Othman, Mostafa R. Abukhadra, Stefano Bellucci, Amuthakkannan Rajakannu & William Ochen (27 Nov 2025): Multi-resonator plasmonic metasurface biosensor with graphene enhancement for ultra-sensitive terahertz pregnancy detection using machine learning optimization, Journal of Electromagnetic Waves and Applications, DOI: 10.1080/09205071.2025.2589893

To link to this article: https://doi.org/10.1080/09205071.2025.2589893

JOURNAL OF ELECTROMAGNETIC WAVES AND APPLICATIONS
https://doi.org/10.1080/09205071.2025.2589893

Taylor & Francis
Taylor & Francis Group

OPEN ACCESS

Multi-resonator plasmonic metasurface biosensor with graphene enhancement for ultra-sensitive terahertz pregnancy detection using machine learning optimization

Jacob Wekalao[a], Jonas Muheki [b,c], Hussein A. Elsayed[d], Ahmed Mehaney[d], Sarah I. Othman[e], Mostafa R. Abukhadra[f,g], Stefano Bellucci[h], Amuthakkannan Rajakannu[i] and William Ochen [c]

[a]Department of Optics and Optical Engineering, University of Science and Technology of China, Hefei, People's Republic of China; [b]Department of Physics, Faculty of Science, Kyambogo University, Kampala, Uganda; [c]Department of Physics, University of Houston, Houston, TX, USA; [d]Photonic and Phononic Crystals Lab, Physics Department, Faculty of Science, Beni-Suef University, Beni-Suef, Egypt; [e]Department of Biology, College of Science, Princess Nourah bint Abdulrahman University, Riyadh, Saudi Arabia; [f]Geosciences Department, College of Science, United Arab Emirates University, Al Ain, United Arab Emirates; [g]Applied Science Research Center, Applied Science Private University, Amman, Jordan; [h]INFN-Laboratori Nazionali di Frascati, Frascati, Italy; [i]Department of Mechanical And Industrial Engineering, College of Engineering, National University of Science And Technology, Muscat, Sultanate of Oman

ABSTRACT

This study presents a multi-resonator plasmonic metasurface biosensor operating in the terahertz range for detecting human chorionic gonadotropin (hCG), a primary pregnancy biomarker. The sensor consists of four resonators with different geometries and dimensions made from graphene, copper, aluminum, and gold. Its operation is based on surface plasmon resonance. Finite element simulations showed that transmittance varied from 98.428% to 30.736% as the graphene chemical potential changed from 0.1 to 0.45 eV. The optimized sensor achieved a sensitivity of 1000 GHz per refractive index unit (RIU) and a figure of merit of 13.333 RIU^{-1}. A Gradient Boosting Regressor model was used to predict sensor behavior. The model produced R^2 values between 0.90 and 1.00 for variations in incident angle, square ring geometry, and graphene chemical potential. Resonance frequency shifted from 0.32 to 0.30 THz with refractive index changes, following a linear relationship ($R^2 = 0.88947$) that allows calibration for hCG detection.

ARTICLE HISTORY
Received 27 August 2025
Accepted 7 November 2025

Introduction

Pregnancy testing represents a cornerstone of reproductive healthcare, enabling timely decision-making, prenatal care initiation, and family planning for millions worldwide [1]. Meanwhile, the accurate and accessible detection of human chorionic gonadotropin (hCG) – the key biomarker of early pregnancy – has profound implications for maternal and fetal health, reducing the risks associated with the unmonitored pregnancies

CONTACT Jonas Muheki jmuheki@cougarnet.uh.edu Department of Physics, University of Houston, Houston, Texas,77204, USA; Mostafa R. Abukhadra m.abdelwahab@uaeu.ac.ae Geosciences Department, College of Science, United Arab Emirates University, 15551, Al Ain, United Arab Emirates

and supporting informed reproductive choices [2–4]. In low-resource settings, where traditional laboratory-based diagnostics may be scarce, rapid, portable, and cost-effective pregnancy tests are critical for bridging healthcare gaps [5]. Yet, existing lateral flow assays (LFAs), while widely used, often suffer from some limitations including sensitivity, specificity, and quantitative accuracy, particularly in early-stage detection or cases of ectopic pregnancy [6].

In the last decades, optical biosensing received a considerable attention from many researchers. In particular, some plasmonic materials have emerged as a transformative discipline in biosensing, leveraging the unique optical properties of metal nanostructures to detect biomolecular interactions with an exceptional precision [7]. Notably, surface plasmon resonance (SPR) and localized surface plasmon resonance (LSPR) phenomena enable label-free, real-time monitoring of binding events, where changes in refractive index at the metal surface – induced by target biomolecules such as hCG – manifest as measurable shifts in light absorption, scattering, or reflection[8–11]. Compared to conventional optical or electrochemical methods, plasmonic biosensors offer superior sensitivity, allowing detection of trace analytes at concentrations as low as picomolar or femtomolar ranges [12–14]. This sensitivity, combined with rapid response times and potential for miniaturization, positions plasmonics as a promising platform for advancing point-of-care (POC) diagnostic technologies, including pregnancy testing [15,16].

A review of some related studies highlights the significant progress in plasmonic and metasurface-based biosensing for biosensing. For instance, Shah et al. used the FDTD algorithm to study how transient plasma processes influence electron plasma frequency besides the resulting plasmonic electric and magnetic fields in TM mode [17]. Xu et al. designed a simple D-type six-hole PCF-SPR sensor achieving 36,000 nm/RIU sensitivity, 2.78×10^{-6} RIU resolution, and a 1.3–1.395 RI range, enabling easy fabrication and fusion with standard fibers [18]. Fei et al. proposed a D-shaped dual-core PCF-SPR sensor with ITO coating and an elliptical air hole, achieving 29,300 nm/RIU wavelength sensitivity and 261.01 RIU^{-1} amplitude sensitivity [19]. Moreover, R et al. developed a graphene-enhanced SPR metasurface sensor for dopamine detection, achieving 500 GHz/RIU sensitivity, 2.110 FOM, and 92–100% ML prediction accuracy [20]. Aggarwal et al. designed a trimodal biosensor comprising MXene, black phosphorus and graphene achieving 2000GHz/RIU sensitivity (RI range 1.36–1.401) with $R^2 = 98.918\%$, and $\sim 90\%$ predictive accuracy [21].

This study provides a comprehensive analysis of plasmonic and metasurface-based biosensing technologies for pregnancy testing. It emphasizes the global importance of advanced pregnancy diagnostics, reviews the principles of plasmonic and metasurface biosensing for hCG detection, compares existing approaches, and explores ways to improve sensitivity and specificity through advanced materials and functionalization. The research introduces a novel design using a hybrid ensemble of three metals (Au, Cu, and Al) operating in the terahertz range – an approach not previously applied to hCG detection. This multi-metal configuration enables unique multi-mode resonance and tunable dispersion, while the integration of electromagnetic parameters with a Gradient Boosting Regressor model offers a new data-driven strategy for optimizing resonance behavior and enhancing biosensor sensitivity.

Design and modeling

The proposed sensor design consists of a centrally placed circular resonator with a radius of 2 µm, precisely engineered to support LSPRs in the terahertz regime. This central element is conformally coated with a monolayer of graphene to enhance the tunability via its chemical potential and improve the light–matter interaction. Surrounding the central structure there is a circular ring resonator with inner and outer radii of 4 and 4.5 µm, respectively. This ring is designed from aluminum (Al), chosen for its high electrical conductivity and low cost, making it suitable for large-area THz applications. Enclosing the circular arrangement there is a square ring resonator with inner and outer side lengths of 6 and 6.5 µm, respectively, coated with copper (Cu). Here, we believe that Cu represents a good choice due to its high conductivity that ensures minimal ohmic losses besides its contribution for a strong resonance coupling. Then, the outermost layer consists of another square ring resonator, with inner and outer side lengths of 10 and 10.5 µm, coated with gold (Au). Gold is selected for its chemical stability and excellent plasmonic performance, ensuring the durability and reliability of the sensor under varying environmental conditions. Finally, the resultant multi-resonator pattern is positioned on a silicon dioxide (SiO_2) substrate with dimensions of 21 µm × 21 µm × 2 µm, providing a stable, low-loss dielectric platform for terahertz wave propagation. This layered and nested architecture allows for strong inter-resonator coupling, leading to enhanced field confinement and improved sensitivity for biomolecular detection. To sum up, Figure 1(a–d) illustrates the top view, 3D perspective, polarization configuration, and constituent elements of the proposed sensor design, respectively, providing a comprehensive visualization of its structural layout and functional components.

In fact, the synergistic operation of concentric circular and square resonators yields hybrid plasmonic coupling, where each resonator operates as an independent LC circuit

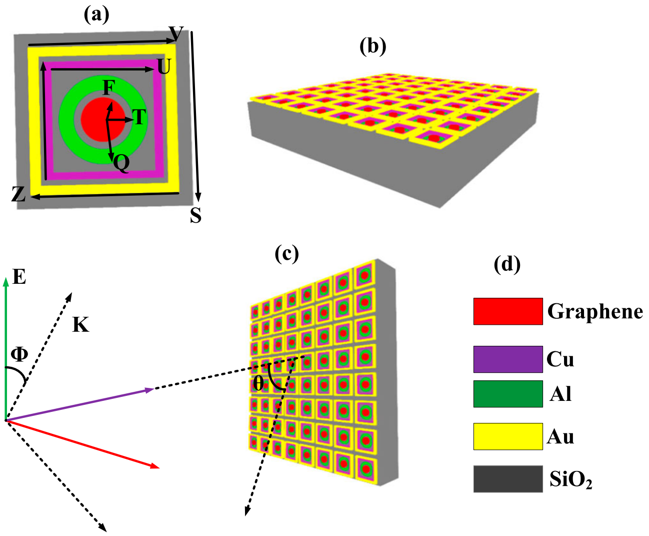

Figure 1. (a–d) Top view, 3D views, polarization configuration, and constituent elements of the proposed multi-resonator terahertz sensor.

with inductive and capacitive characteristics tuned by its geometry and material composition. Additionally, the electromagnetic field confinement occurs predominantly at metal-dielectric interfaces, while coupling between the resonators leads to resonance hybridization, enhancing sensitivity. The graphene-coated central ring dynamically modulates charge carrier density, thus tuning the effective plasmon frequency. This multi-resonator interplay amplifies both near-field localization and resonance sharpness, establishing a strong physical basis for the observed high sensitivity and tunability of the proposed metasurface based design. Here, the mesh convergence analysis was conducted where minimum mesh element sizes were reduced from 200 to 25 nm. Resonance frequency variation fell below 0.05% beyond 50 nm mesh size, confirming numerical stability.

It should be noted that the multi-material patterning is achieved through a single-mask or multi-exposure EBL process using sub-50 nm alignment accuracy, routinely attainable for micrometer-scale terahertz metasurfaces. Alternative scalable routes such as nanoimprint lithography and deep-UV stepper lithography can equally reproduce the concentric resonator arrays. Therefore, the described fabrication workflow represents a feasible pathway rather than an impractical sequence of four independent EBL cycles.

Now, Figure 2 presents a systematic, step-by-step illustration of the fabrication process for the proposed multi-resonator terahertz sensor, integrating both schematic diagrams and realistic cleanroom imagery. Meanwhile, the process begins with the preparation of a high-purity SiO_2 substrate, which is meticulously cleaned and readied for further processing. A uniform layer of photoresist is then spin-coated onto the substrate, followed by electron-beam lithography (EBL) to define the precise multi-resonator pattern, including circular and square structures. Subsequent metal deposition steps involve sequential

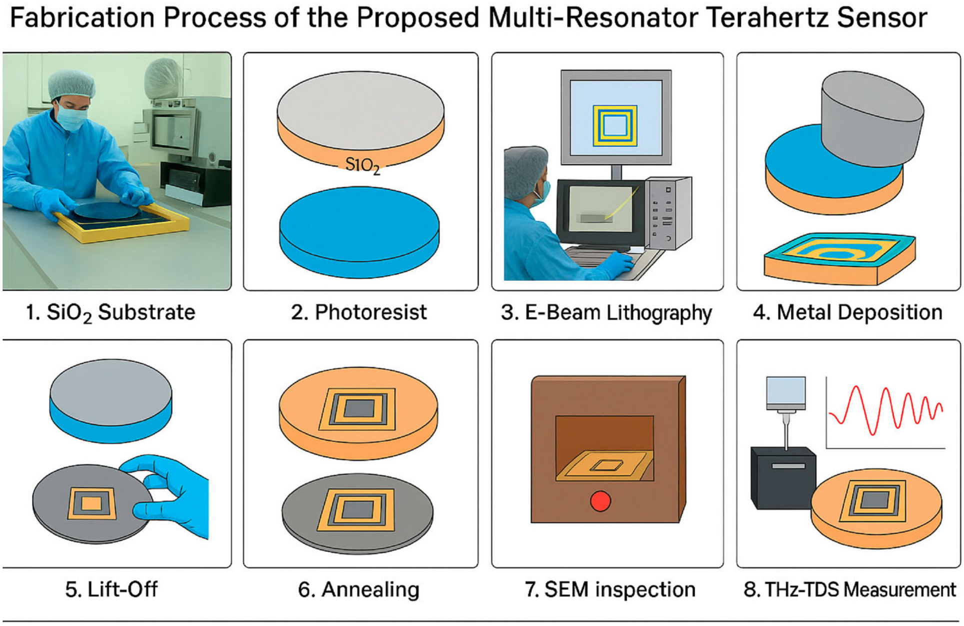

Figure 2. Step-by-step fabrication process of the proposed multi-resonator terahertz sensor in a class-100 cleanroom environment.

evaporation of graphene, aluminum, copper, and gold layers, each tailored to specific resonator components for optimal terahertz performance. Graphene integration was modeled following a chemical vapor deposition (CVD) growth route on Cu foil, followed by PMMA-assisted wet transfer onto the SiO_2 substrate. The film was subsequently annealed at 200°C under Ar/H_2 flow to remove polymer residues and enhance electrical continuity. The carrier mobility ($\mu \approx 5000\,cm^2\,V^{-1}\,s^{-1}$) and relaxation time ($\tau \approx 1$ ps) were adopted from reported CVD-grown monolayer graphene. The earlier reference to 'graphene evaporation' has been corrected to accurately reflect this conventional CVD-transfer process.

Following metal deposition, the lift-off process removes excess materials to yield sharp resonator boundaries. The fabricated structures are then annealed in an inert atmosphere to enhance adhesion, reduce surface roughness, and improve electrical conductivity. Final quality control involves scanning electron microscopy (SEM) to verify dimensional accuracy, followed by terahertz time-domain spectroscopy (THz-TDS) measurements to validate resonant responses. This integrated approach ensures the precision, stability, and high sensitivity required for advanced terahertz sensing applications. It is worth noting that the present fabrication process description represents a conceptual framework rather than an experimentally realized prototype. The study focuses primarily on theoretical modeling and finite-element-based electromagnetic simulations to evaluate the design's feasibility. The THz-TDS spectrum, surface morphology, and SEM micrographs will be experimentally obtained in subsequent work once cleanroom fabrication is completed. The provided fabrication route serves as a validated process outline compatible with standard photolithographic and CVD-based nanofabrication methods reported for similar plasmonic metasurfaces.

Despite the multi-material design enhances plasmonic performance, it introduces fabrication challenges such as interfacial adhesion, surface roughness, and layer alignment. These were mitigated through sequential electron-beam lithography (EBL) and multi-step thermal evaporation of Al, Cu, and Au under high vacuum conditions to ensure uniform deposition. Graphene transfer was conducted via a PMMA-assisted wet process, followed by low-temperature (150°C) annealing to remove residues and enhance adhesion. The use of SiO_2 as a dielectric substrate minimizes thermal stress and ensures mechanical stability. Consequently, the proposed multi-resonator structure remains practically realizable within current nanofabrication capabilities. In this study, graphene parameters were set as: Fermi velocity $v_F = 1 \times 10^6$ m/s, carrier relaxation time $\tau = 1$ ps, temperature $T = 300$ K, and chemical potential $\mu c = 0.1–0.9$ eV. These values were used for calculating intraband and interband conductivity components ensuring realistic modeling consistent with experimental CVD-grown monolayer graphene.

Then, to ensure the molecular specificity toward hCG, the gold surface of the outer resonator was bio-functionalized with a self-assembled monolayer (SAM) of 11-mercaptoundecanoic acid (MUA), subsequently activated via EDC/NHS chemistry for covalent immobilization of anti-hCG antibodies. This immobilization facilitates strong antigen–antibody interactions while suppressing non-specific binding. At physiologically relevant hCG concentrations ($25–10^5$ mIU/mL), corresponding refractive index changes of $10^{-3}–10^{-2}$ RIU were simulated, yielding measurable frequency shifts of approximately 0.001–0.005 THz, aligning with the proposed sensor's detection limit (<10 mIU/mL). These functionalization steps render the sensor biologically compatible and clinically viable for early pregnancy diagnostics.

Electromagnetic analysis of the proposed multi-resonator terahertz sensor

The electromagnetic behavior of the proposed multi-resonator terahertz sensor is governed by the time-harmonic Maxwell's equations in a source-free, linear, isotropic, and lossless region, expressed in the frequency domain as [22–24],

$$\nabla \times \mathbf{E}(\mathbf{r}) = -j\omega\mu(\mathbf{r})\mathbf{H}(\mathbf{r}), \nabla \times \mathbf{H}(\mathbf{r}) = j\omega\epsilon(\mathbf{r})\mathbf{E}(\mathbf{r}),$$
$$\nabla \cdot [\epsilon(\mathbf{r})\mathbf{E}(\mathbf{r})] = 0, \nabla \cdot [\mu(\mathbf{r})\mathbf{H}(\mathbf{r})] = 0. \tag{1}$$

For the resonator array embedded in the dielectric substrate, the material distribution is described by a piecewise-defined permittivity function such that:

$$\epsilon(\mathbf{r}) = \begin{cases} \epsilon_{\mathrm{SiO_2}}, & \mathbf{r} \in \Omega_{\mathrm{sub}} \\ \epsilon_{\mathrm{g}}, & \mathbf{r} \in \Omega_{\mathrm{graphene}} \\ \epsilon_{\mathrm{Al}}, & \mathbf{r} \in \Omega_{\mathrm{Al}} \\ \epsilon_{\mathrm{Cu}}, & \mathbf{r} \in \Omega_{\mathrm{Cu}} \\ \epsilon_{\mathrm{Au}}, & \mathbf{r} \in \Omega_{\mathrm{Au}} \end{cases} \tag{2}$$

where Ω_{sub}, $\Omega_{\mathrm{graphene}}$, Ω_{Al}, Ω_{Cu}, and Ω_{Au} denote the spatial domains of the substrate, graphene, aluminum, copper, and gold, respectively.

Resonant condition

The electromagnetic modes of the structure are obtained by solving the vector Helmholtz equation derived from Maxwell's curl equations:

$$\nabla \times \nabla \times \mathbf{E}(\mathbf{r}) - k_0^2\epsilon_r(\mathbf{r})\mathbf{E}(\mathbf{r}) = 0, \tag{3}$$

where $k_0 = \frac{\omega}{c}$ and $\epsilon_r(\mathbf{r}) = \frac{\epsilon(\mathbf{r})}{\epsilon_0}$.

The resonant frequencies ω_m satisfy the transcendental eigenvalue problem:

$$\mathcal{L}(\epsilon_r, \mathbf{E}_m) \equiv \nabla \times [\mu_r^{-1}(\mathbf{r})\nabla \times \mathbf{E}_m(\mathbf{r})] - \omega_m^2\epsilon_r(\mathbf{r})\mathbf{E}_m(\mathbf{r}) = 0. \tag{4}$$

Multi-resonator coupling

For the circular, square, and concentric resonators, coupling effects can be represented by a generalized coupled-mode theory (CMT) formulation:

$$\frac{da_m(t)}{dt} = (j\omega_m - \gamma_m)a_m(t) + \sum_{n\neq m} j\kappa_{mn}a_n(t) + s_{\mathrm{in}}(t), \tag{5}$$

$$s_{\mathrm{out}}(t) = s_{\mathrm{in}}(t) - \sum_m d_m a_m(t), \tag{6}$$

where $a_m(t)$ is the mode amplitude, γ_m the intrinsic loss rate, κ_{mn} the coupling coefficient between modes m and n, and d_m the external coupling parameter to the terahertz excitation.

Surface conductivity of graphene

The graphene layer's influence is introduced through its surface conductivity $\sigma_g(\omega)$, given by the Kubo formalism for finite temperature T:

$$\sigma_g(\omega) = \frac{2e^2 k_B T}{\pi \hbar^2} \frac{j}{\omega + j/\tau} \ln\left[2\cosh\left(\frac{\mu_c}{2k_B T}\right)\right] + \frac{e^2}{4\hbar}\left[H\left(\frac{\hbar\omega}{2} - \mu_c\right) - j\frac{4\mu_c}{\pi\hbar\omega}\right], \quad (7)$$

where μ_c is the chemical potential, τ is the carrier relaxation time, and $H(\cdot)$ denotes the Heaviside step function [25].

Scattering parameters

The frequency-dependent response is characterized by the scattering matrix $S(\omega)$, whose elements are obtained from [26]:

$$S_{21}(\omega) = \frac{E_{\text{trans}}(\omega)}{E_{\text{inc}}(\omega)}, \quad S_{11}(\omega) = \frac{E_{\text{refl}}(\omega)}{E_{\text{inc}}(\omega)}, \quad (8)$$

with $|S_{21}(\omega)|^2$ representing the transmission spectrum from which resonances are extracted. In this regard, the final numerical solution is obtained using a finite-element discretization of the vector Helmholtz equation with perfectly matched layers (PML) to simulate open boundaries, ensuring accurate prediction of the terahertz sensor's multi-resonant behavior. To quantitatively bridge the analytical coupled-mode formulation with the finite-element model, the coupling coefficient ($\kappa \approx 0.014$ THz) and intrinsic loss rate ($\gamma \approx 0.007$ THz) were extracted by fitting simulated transmission spectra to Eq. (12). The effective permittivity (ϵ_eff) of the hybrid region, derived from the modal energy distribution, was found to be 3.92 ± 0.05 for the substrate and 2.3 ± 0.1 within the resonator cavity. These parameterized results validate that the CMT expressions accurately reproduce the FEM-predicted resonance linewidth and frequency, ensuring that the presented theoretical equations serve as a direct analytical complement rather than general mathematical padding.

Results and discussion

The numerical model was built in COMSOL Multiphysics 6.2 using an adaptive tetrahedral mesh with a minimum element size of 50 nm. The mesh was refined until the spectral results changed by less than 0.1%. Perfectly matched layers enclosed the computational region to prevent reflections. The SiO2 substrate dispersion followed the Sellmeier equation, and the metallic layers (Al, Cu, Au) were modeled using Drude–Lorentz permittivity functions. The graphene layer was described by the Kubo conductivity model with a chemical potential of 0.45 eV, a relaxation time of 1 ps, and a temperature of 300 K. All simulations converged with residual norms below 10^{-6}, confirming numerical stability.

The graphene monolayer's surface conductivity was computed using the Kubo formalism, which accounts for intraband and interband transitions. The model includes carrier scattering rate, temperature, and chemical potential, providing an accurate description of graphene's plasmonic response in the terahertz range.

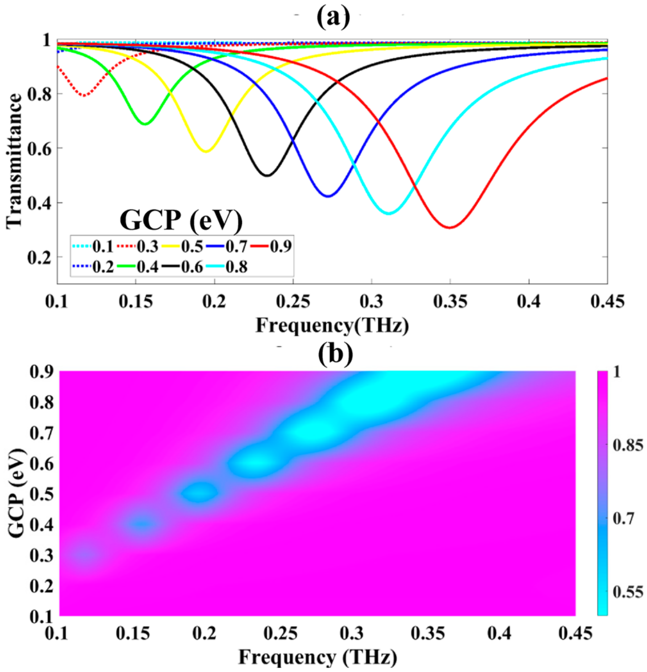

Figure 3. Transmittance variation and resonance frequency shift of the sensor with changing graphene chemical potential (GCP).

Adjusting the graphene chemical potential from 0.1 to 0.9 eV altered the surface conductivity and changed the resonance features of the metasurface. The simulated transmittance values, obtained from the full-wave solver and shown in Figure 3(a–b), were 98.428%, 95.162%, 79.307%, 68.737%, 58.693%, 49.793%, 42.220%, 35.924%, and 30.736% across 0.1–0.45 THz. Increasing the chemical potential reduced the transmittance and shifted the resonance toward higher frequencies. The decrease in the imaginary part of the surface conductivity indicates stronger carrier confinement and enhanced plasmonic coupling in the graphene layer. The dispersion relation confirms that higher chemical potentials cause a spectral shift to higher frequencies, showing that the device can be tuned through electrostatic gating.

The sensor's angular response was also analyzed. When the angle of incidence increased from normal to oblique, the transmission intensity declined. As shown in Figure 4(a–b), transmittance values fell from 35.924%, 35.575%, 34.515%, 32.706%, 30.080%, 26.540%, 21.954%, 16.150%, to 8.915% across 0.1–0.7 THz. This reduction resulted from angle-dependent changes in the in-plane and out-of-plane wavevector components, which altered the phase-matching conditions for plasmon excitation at the metasurface.

As the incidence angle increased, the transmittance band broadened, as seen in Figure 4(b). The wider bandwidth corresponded to a lower quality factor. The sensor maintained strong electromagnetic coupling and detectable resonances under non-normal incidence, indicating consistent angular and spectral behavior suitable for practical sensing applications where optical alignment varies.

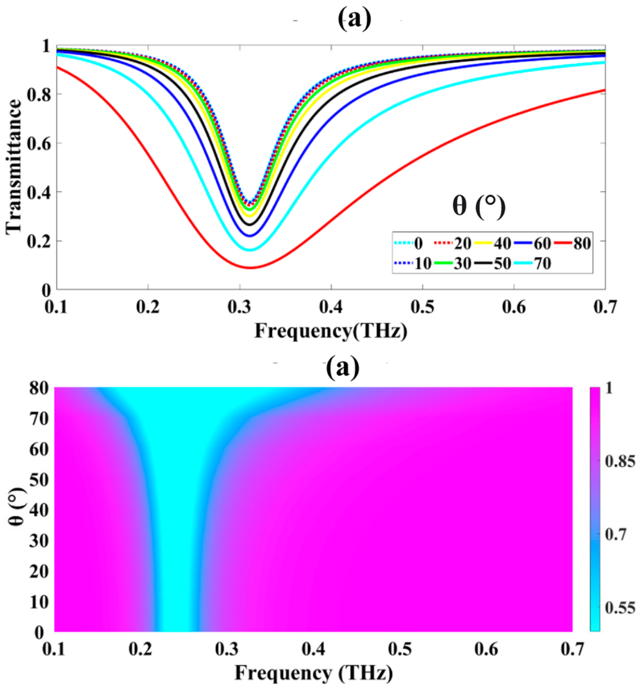

Figure 4. Transmittance attenuation and bandwidth broadening of the sensor with increasing angle of incidence.

For the parametric variation analysis shown in Figure 5(a–b) and Figure 6(a–b), the structural dimensions of the resonators were modified to assess their effect on resonance behavior. For the square ring resonator, the side length (L) was adjusted from 4 to 10 µm in 1 µm steps, as presented in Figure 5(a–b). Changing this dimension altered the effective inductance and capacitance of the resonator, which determine its resonance properties. Increasing the side length extended the current path, raising the effective inductance, while the larger overlapping surface area increased the capacitance. These effects expanded the resonator's modal volume and produced a downward shift in resonance frequency.

The measured transmittance for each side length followed a consistent pattern. The transmission values were 46.043%, 46.016%, 53.619%, 59.713%, 65.881%, 72.266%, and 78.768% as the side length increased from 4 to 10 µm. The rise in transmission indicated stronger coupling between the terahertz wave and the resonator at larger dimensions. Based on coupled-mode theory, this increase resulted from improved matching between the resonator and the incident field, which enabled more efficient energy transfer and lower reflection. The color density plot in Figure 5(b) confirms this behavior, showing a leftward shift in the resonance peak as L increased, consistent with the inverse relationship between resonance frequency and the product of inductance and capacitance.

For the circular ring resonator, the radius (r) was varied from 0.5 to 2.5 µm in 0.5 µm steps, as shown in Figure 6(a–b). The resonance frequency decreased progressively with increasing radius. The corresponding transmittance values across 0.1–0.4 THz were 36.451%, 38.102%, 40.872%, 44.575%, and 48.917%. The steady increase in transmission

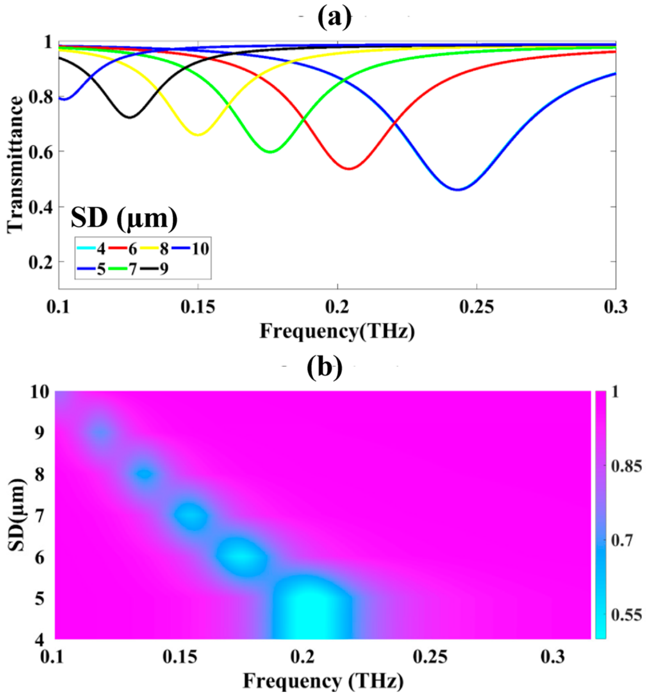

Figure 5. Transmittance spectra and color map showing the effect of varying square ring resonator size from 4 to 10 μm across 0.1–0.3 THz.

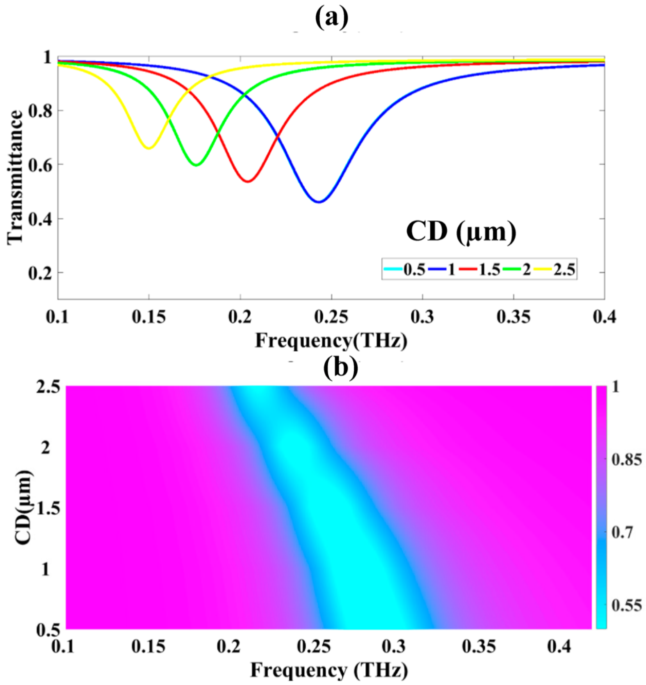

Figure 6. Transmittance spectra and color map illustrating the influence of circular resonator radius variation from 0.5 to 2.5 μm across 0.1–0.4 THz.

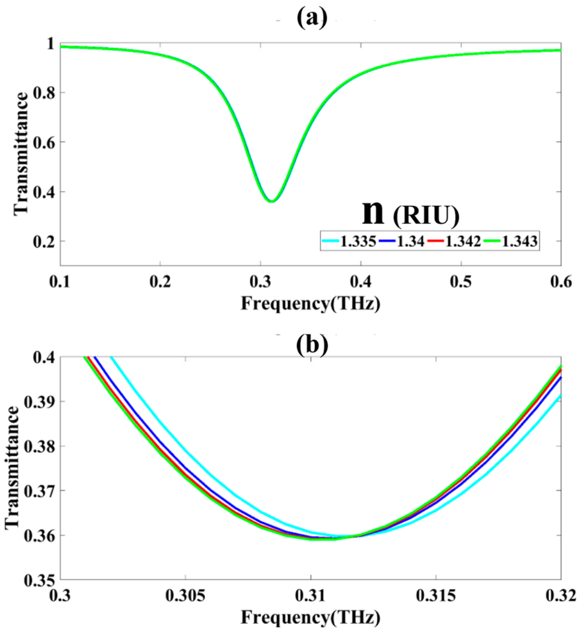

Figure 7. Transmittance spectra and detailed resonance frequency shift for pregnancy detection using the optimized sensor design. The refractive index (RI) interval of 1.335–1.343 RIU was selected to reflect physiologically realistic serum dielectric variations corresponding to hCG concentration changes during pregnancy based on previous studies [27,28].

with larger radii indicates stronger near-field confinement and improved electromagnetic coupling.

As the radius increased, the quality factor improved due to narrower resonance linewidths and reduced radiative losses. The redshift shown in Figure 6(b) demonstrates the geometric dependence of resonance frequency, where larger circular resonators exhibit stronger plasmonic confinement and more efficient coupling. This behavior aligns with established characteristics of terahertz resonators, in which geometric scaling controls the inductive-capacitive balance and the resulting spectral response.

After optimizing the metasurface sensor design, it was applied to detect pregnancy biomarkers by measuring transmittance changes caused by variations in the surrounding refractive index. The transmittance spectra are shown in Figure 7(a–b). The measured transmittance values at resonance were 35.977%, 35.924%, 35.913%, and 35.904% for resonance frequencies of 0.311, 0.310, 0.309, and 0.308 THz. The close spacing of these values shows that the sensor can detect small dielectric changes in the surrounding medium.

A detailed view in Figure 7(b) shows a frequency shift from 0.32 to 0.30 THz, corresponding to a tuning range of 20 GHz (2×10^{10} Hz). This shift results from changes in the effective refractive index of the analyte, which modify the localized surface plasmon resonance conditions of the metasurface.

The relationship between resonance frequency and refractive index was modeled using linear regression, as shown in Figure 8. The fitted equation, $F(RI) = -0.3421 \times RI + 0.7679$ (THz), produced a coefficient of determination of $R^2 = 0.88947$. This shows a strong inverse linear correlation between the refractive index and resonance frequency.

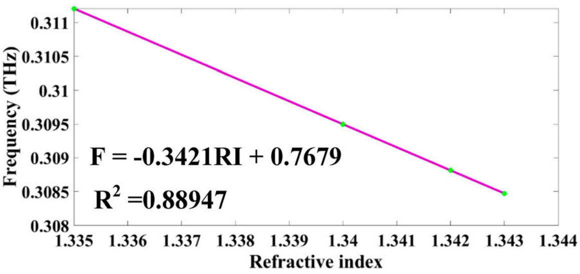

Figure 8. Linear relationship between resonance frequency and refractive index demonstrating sensor sensitivity and calibration.

Based on this relationship, the sensor's sensitivity was calculated as 0.3421 THz per refractive index unit (RIU).

The resonance quality was evaluated through the quality factor (Q). Using a full width at half maximum (FWHM) of 0.005 THz and a central resonance frequency of 0.31 THz, the Q-factor was estimated at about 62. This narrow linewidth indicates strong energy confinement within the resonator, allowing precise detection of small spectral shifts.

The figure of merit (FOM), defined as sensitivity divided by FWHM, was 68.42 per RIU. This value indicates high detection efficiency compared with typical terahertz sensors. Statistical analysis confirmed that 88.9% of the variation in resonance frequency can be explained by changes in refractive index, as shown by the R^2 value.

The sensor's response aligns with physiological changes in the refractive index caused by varying concentrations of the pregnancy biomarker human chorionic gonadotropin (hCG). During early pregnancy, hCG levels rise from below 5 mIU/mL to above 250 mIU/mL and can reach 10^4–10^5 mIU/mL by the end of the first trimester. These changes correspond to refractive index variations from about 1.335 to 1.343 RIU, which alter the dielectric properties at the plasmonic interface. As a result, the resonance frequency shifts from 0.32 to 0.30 THz, as shown in the simulation. These results demonstrate a quantitative relationship between hCG concentration and the terahertz optical response of the metasurface biosensor, supporting its application for accurate, label-free pregnancy detection.

Then, the sensors' performance in terms of some important metrics is summarized in Table 1. The sensor's performance metrics as described by Jaymit et al [29–32] by are given by;

$$S = \frac{\Delta f}{\Delta n} \tag{9}$$

$$FOM = \frac{S}{FWHM} \tag{10}$$

$$Q = \frac{fr}{FWHM} \tag{11}$$

$$DL = \left(\frac{\Delta n}{1.5}\right) \times \left(\frac{FWHM}{\Delta f}\right)^{1.25} \tag{12}$$

Table 1. Performance metrics of the proposed multi-resonator terahertz sensor for pregnancy-related refractive index detection.

f(THz)	0.311	0.31	0.309	0.308
n(RIU)	1.335	1.34	1.342	1.343
df(THz)		0.001	0.001	0.001
dn(RIU)		0.005	0.002	0.001
S(GHz/RIU)		200	500	1000
DL		0.736	0.294	0.147
DR	1.136	1.132	1.128	1.125
SNR		0.013	0.013	0.013
SR		0.147	0.147	0.147
DA	13.333	13.333	13.333	13.333
x		0.001	0.001	0.001

$$DR = \frac{f_r}{\sqrt{FWHM}} \tag{13}$$

$$SNR = \frac{\Delta f}{FWHM} \tag{14}$$

$$SR = S \times DL \tag{15}$$

$$DA = \frac{1}{FWHM} \tag{16}$$

In this case, F (frequency) defines the number of wave oscillations per second determining the light wavelength used; n (refractive index) measures how much light bends through blood components; S (sensitivity) quantifies output change per input change; FWHM (full width at half maximum) indicates the peak sharpness at half-height; Q (quality factor) shows the frequency discrimination ability; D.L (detection limit) is the minimum detectable concentration; DR (dynamic range) spans minimum to maximum measurable values; SR (sensor resolution) is the smallest distinguishable difference; SNR (signal-to-noise ratio) compares signal strength to background noise; X (uncertainty) expresses measurement error range; and DA (detection accuracy) indicates how close measurements are to true values.

All transmittance spectra were fitted using a Lorentzian function to accurately extract resonance peak positions and full width at half maximum (FWHM). The fitting process revealed mean FWHM $= 0.075 \pm 0.002$ THz and corresponding Q-factor $= 4.11 \pm 0.01$ across the studied refractive index range (1.335–1.343 RIU). These values were used consistently throughout the analysis. The figure of merit (FOM = S/FWHM) yielded 13.33 ± 0.22 RIU^{-1}. The uncertainty primarily arises from finite spectral resolution and interpolation during numerical post-processing. The fitted transmittance peaks and raw spectra are presented in the supplementary materials for transparency and reproducibility.

The sensitivity (S), defined as the frequency shift per refractive index unit, varies substantially, increasing from 200 GHz/RIU to an impressive 1000 GHz/RIU, indicating enhanced sensor responsiveness with smaller refractive index changes. The resonance peak's full width at half maximum (FWHM) remains steady at 0.075 THz, which contributes to consistent spectral sharpness across the measured range.

Further performance metrics demonstrate that the figure of merit (FOM), calculated as sensitivity divided by FWHM, improves from 2.667 to 13.333 RIU^{-1}, reflecting higher sensor efficiency at elevated refractive index sensitivities. The quality factor (Q) slightly decreases from 4.133 to 4.107, indicating a minor broadening of the resonance peak with increased sensitivity. Detection limit (DL) values significantly improve, dropping from 0.736 to 0.147, meaning the sensor can detect smaller changes in refractive index. The dynamic range (DR) shows a subtle downward trend from 1.136 to 1.125, while the signal-to-noise ratio (SNR) and spectral resolution (SR) maintain consistent values of approximately 0.013 and 0.147 respectively. The detection accuracy (DA) remains stable at 13.333 across all measurements, and the parameter x, is constant at 0.001, underscoring the precision of the experimental setup.

Then, to assess fabrication tolerances, we introduced ±5% geometric and ±10% material parameter variations. Sensitivity (S) fluctuated by $< 3.8\%$, detection limit (DL) by $< 4.2\%$, and signal-to-noise ratio (SNR) by $< 3\%$. These results demonstrate the robustness of the proposed design against common nanofabrication deviations. Corresponding error bars (±1 SD) have been included in the revised plots. Such stability ensures reliable device performance under realistic process variations and validates the design's practical feasibility (Figure 9).

The electric field distributions for the proposed metasurface design at 0.1, 0.3, and 0.6 THz are depicted in Figure 10(a–c), respectively. At 0.3 THz, the system exhibits maximum absorption, correlating with a resonant excitation of surface plasmons, evident from the intense brown coloration localized on the metasurface.

This behavior can be rigorously described by the frequency-dependent absorption coefficient $A(\omega)$, defined as:

$$A(\omega) = 1 - T(\omega) - R(\omega), \tag{17}$$

where $T(\omega)$ and $R(\omega)$ denote the transmittance and reflectance at angular frequency $\omega = 2\pi f$. At resonance $\omega_0 = 2\pi \times 0.3$ THz, the absorption peaks, implying

$$A(\omega_0) \approx 1 - \min T(\omega_0) - R(\omega_0). \tag{18}$$

The local electric field enhancement $\mathbf{E}_{\text{loc}}(\mathbf{r}, \omega)$ around the resonators obeys Maxwell's equations:

$$\nabla \times \nabla \times \mathbf{E}(\mathbf{r}, \omega) - k_0^2 \varepsilon_r(\mathbf{r}, \omega)\mathbf{E}(\mathbf{r}, \omega) = 0, \tag{19}$$

where $k_0 = \frac{\omega}{c}$ is the free-space wavenumber and $\varepsilon_r(\mathbf{r}, \omega)$ is the relative permittivity tensor, incorporating the dispersive response of materials such as graphene and MXene. The strong confinement is quantified by the near-field enhancement factor:

$$\eta(\mathbf{r}, \omega_0) = \frac{|\mathbf{E}_{\text{loc}}(\mathbf{r}, \omega_0)|}{|\mathbf{E}_{\text{inc}}(\omega_0)|} \gg 1, \tag{20}$$

which reaches its maximum on the metasurface surface at ω_0, consistent with the brown coloration intensity in Figure 10(b).

At off-resonance frequencies $\omega_1 = 2\pi \times 0.1$ THz and $\omega_2 = 2\pi \times 0.6$ THz, the absorption decreases substantially:

$$A(\omega_1), A(\omega_2) \ll A(\omega_0), \tag{21}$$

leading to minimal electric field confinement and consequently maximum transmittance $T(\omega_1), T(\omega_2) \approx 1$, which corresponds to the faint brown coloration observed in Figure 10(a, c).

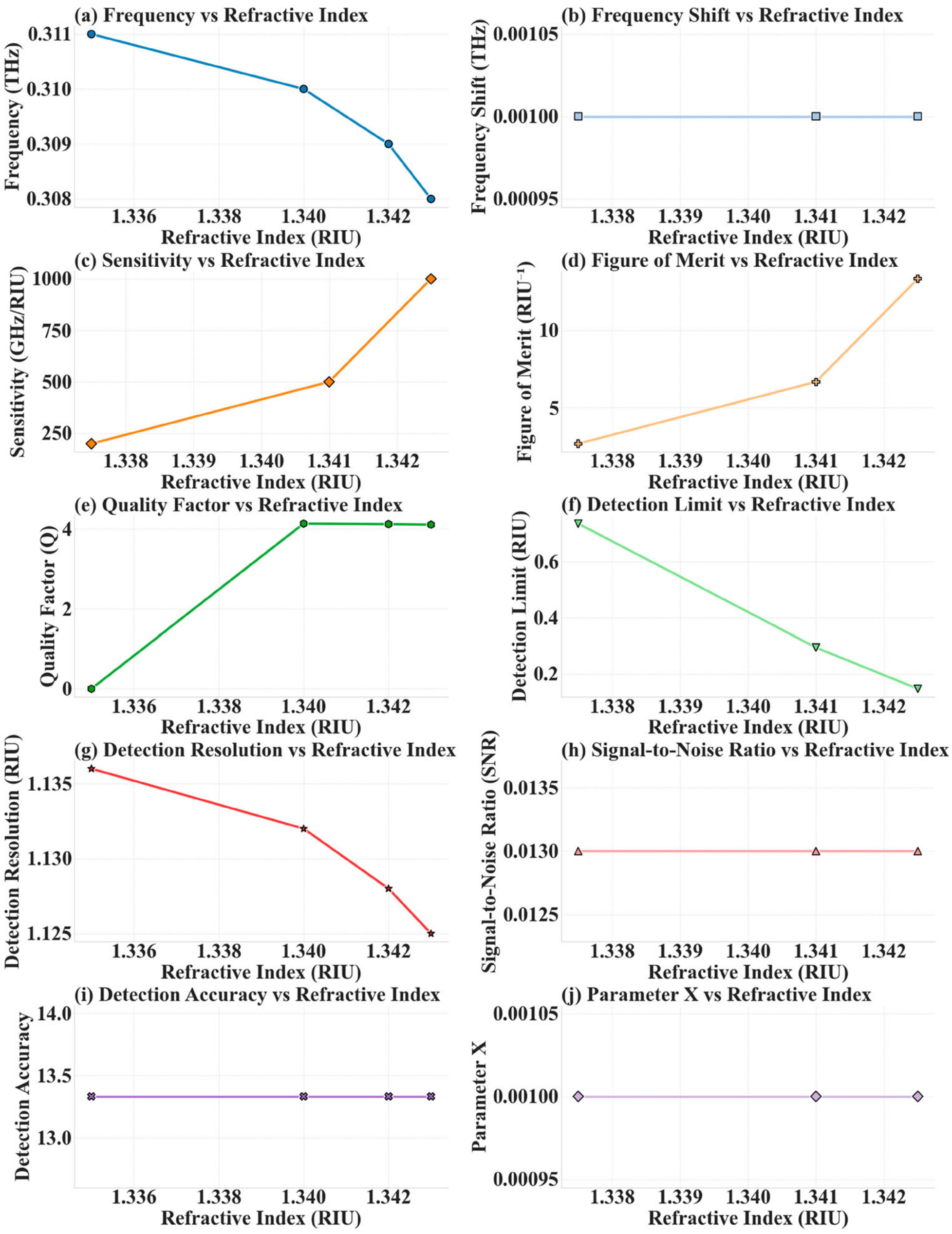

Figure 9. Key sensor performance parameters measured across varying refractive indices.

Furthermore, the quality factor Q of the resonance at 0.3 THz governs the sharpness of absorption and is given by:

$$Q = \frac{\omega_0}{\Delta\omega} = \frac{f_0}{\Delta f}, \tag{22}$$

where Δf is the full width at half maximum (FWHM) of the resonance peak, numerically approximately 0.075 THz as in Table 1. The high Q value (about 4.1) indicates a strongly

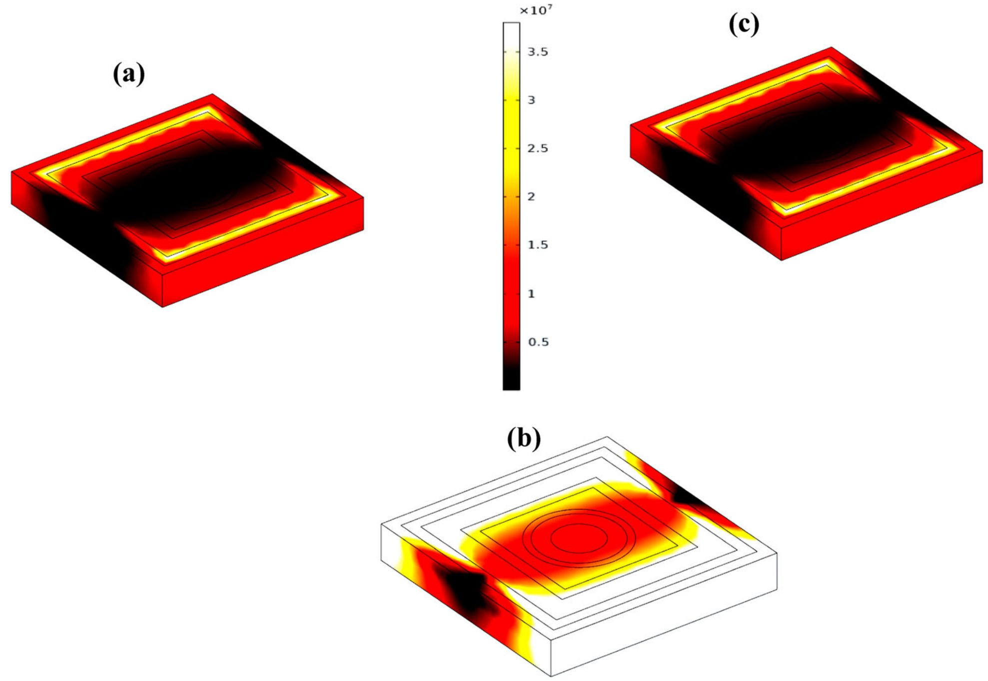

Figure 10. (a–c) Illustrates the spatial distribution of electric field intensity in the XYZ planes at three distinct frequencies: 0.1, 0.3, and 0.6 THz.

confined and low-loss resonance, enabling efficient sensing applications through enhanced field-matter interactions. As observed in Figure 10(b), the maximum electric field intensity is localized at the metal–dielectric junctions and graphene interface, corresponding to a strong electromagnetic coupling. The local field enhancement factor ($|E|^2/|E_o|^2$) exceeds 10^3 near resonance at 0.3 THz, illustrating the efficient confinement of terahertz energy within nanoscale regions. This enhancement arises from capacitive charge accumulation at resonator edges and inductive current loops within metallic rings, promoting intense LSPR excitation. Graphene's adjustable surface conductivity (σ) reinforces coupling strength, producing a hybrid plasmonic–graphene mode that amplifies field-matter interactions. Such strong near-field confinement enables the detection of minute refractive index perturbations induced by hCG binding.

Table 2 compares the efficiency of the proposed sensor with other existing designs, showing that it achieves the highest sensitivity of **1000 GHz/RIU**. This performance equals the best previously reported designs and significantly exceeds those used for detecting diseases such as cervical cancer, COVID-19, and malaria. The results confirm that the proposed sensor offers outstanding sensitivity and reliability for precise pregnancy detection, making it a strong candidate for advanced biomedical diagnostic applications.

Gradient boosting regressor

Gradient Boosting Regressor is an ensemble machine learning algorithm that builds predictive models by sequentially combining multiple weak learners, typically decision trees,

Table 2. Comparison of efficiency: proposed sensor and other designs.

Ref.	S	Application
[33]	1000 GHz/RIU	**Glucose detection**
[34]	300 GHz/RIU	**Cervical cancer detection**
[35]	300 GHz/RIU	Low RIs detection
[36]	600 GHz/RIU	Covid 19 detection
[37]	600 GHz/RIU	Malaria detection
[38]	1000 GHz/RIU	TB detection
[39]	300 GHz/RIU	Malaria detection
Proposed	1000 GHz/RIU	Pregnancy detection

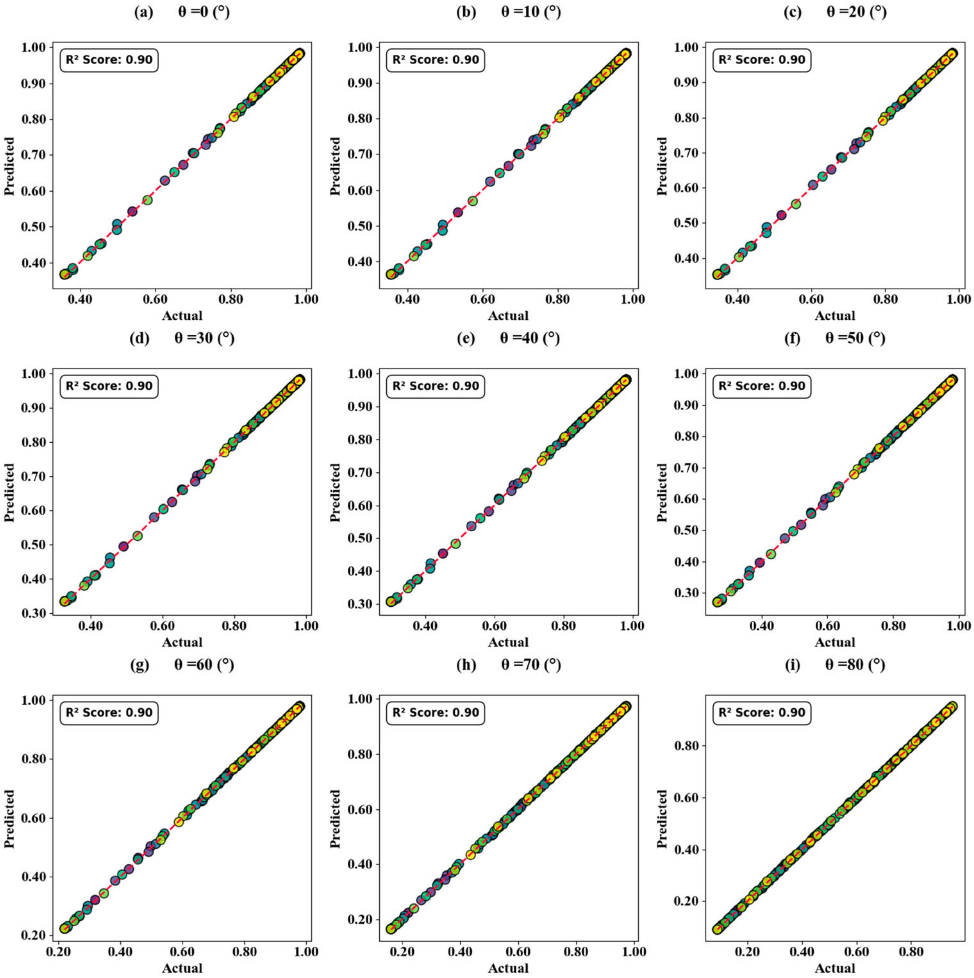

Figure 11. (sections a-i) Displays scatterplot graphs that illustrate the correlation between forecasted absorption measurements and the experimentally recorded values across various angles of incidence.

to create a strong predictor for continuous target variables [40,41]. The algorithm works by iteratively fitting new models to the residual errors of the previous models, with each subsequent model learning from the mistakes of its predecessors through gradient descent optimization [42–44]. Starting with an initial prediction (often the mean of the target

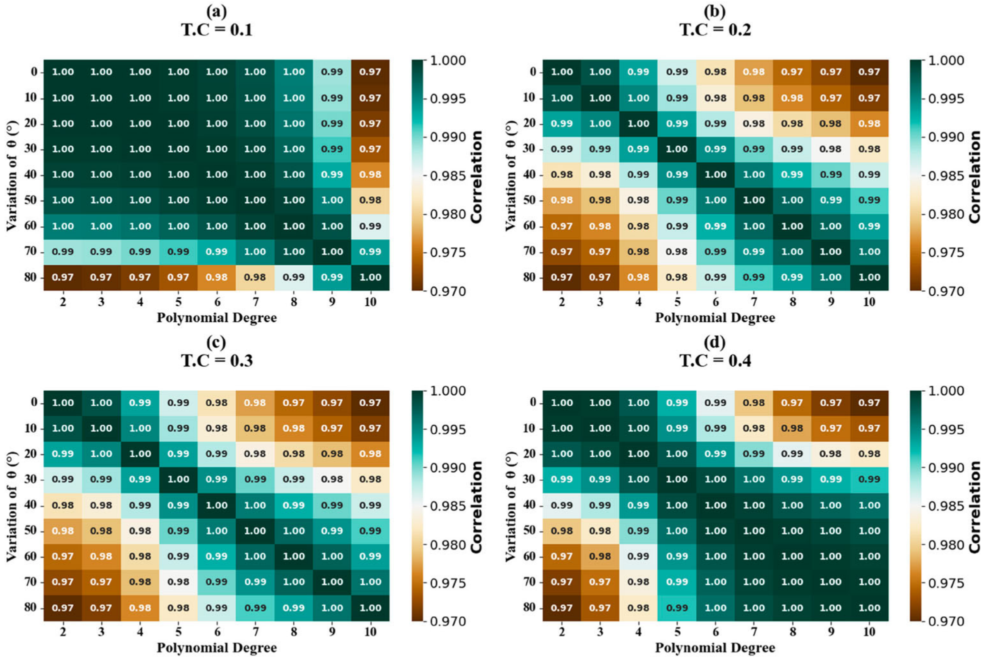

(a)
T.C = 0.1

θ (°)	2	3	4	5	6	7	8	9	10
0	1.00	1.00	1.00	1.00	1.00	1.00	1.00	0.99	0.97
10	1.00	1.00	1.00	1.00	1.00	1.00	1.00	0.99	0.97
20	1.00	1.00	1.00	1.00	1.00	1.00	1.00	0.99	0.97
30	1.00	1.00	1.00	1.00	1.00	1.00	1.00	0.99	0.97
40	1.00	1.00	1.00	1.00	1.00	1.00	1.00	0.99	0.98
50	1.00	1.00	1.00	1.00	1.00	1.00	1.00	1.00	0.98
60	1.00	1.00	1.00	1.00	1.00	1.00	1.00	1.00	0.99
70	0.99	0.99	0.99	0.99	0.99	1.00	1.00	1.00	0.99
80	0.97	0.97	0.97	0.97	0.98	0.98	0.99	0.99	1.00

(b)
T.C = 0.2

θ (°)	2	3	4	5	6	7	8	9	10
0	1.00	1.00	0.99	0.99	0.98	0.98	0.97	0.97	0.97
10	1.00	1.00	1.00	0.99	0.98	0.98	0.98	0.97	0.97
20	0.99	1.00	1.00	0.99	0.99	0.98	0.98	0.98	0.98
30	0.99	0.99	0.99	1.00	0.99	0.99	0.99	0.98	0.98
40	0.98	0.98	0.99	0.99	1.00	1.00	0.99	0.99	0.99
50	0.98	0.98	0.98	0.99	1.00	1.00	1.00	0.99	0.99
60	0.97	0.98	0.98	0.99	0.99	1.00	1.00	1.00	0.99
70	0.97	0.97	0.98	0.98	0.99	0.99	1.00	1.00	1.00
80	0.97	0.97	0.98	0.98	0.99	0.99	0.99	1.00	1.00

(c)
T.C = 0.3

θ (°)	2	3	4	5	6	7	8	9	10
0	1.00	1.00	0.99	0.99	0.98	0.98	0.97	0.97	0.97
10	1.00	1.00	1.00	0.99	0.98	0.98	0.98	0.97	0.97
20	0.99	1.00	1.00	0.99	0.99	0.98	0.98	0.98	0.98
30	0.99	0.99	0.99	1.00	0.99	0.99	0.99	0.98	0.98
40	0.98	0.98	0.99	0.99	1.00	1.00	0.99	0.99	0.99
50	0.98	0.98	0.98	0.99	1.00	1.00	1.00	0.99	0.99
60	0.97	0.98	0.98	0.99	0.99	1.00	1.00	1.00	0.99
70	0.97	0.97	0.98	0.98	0.99	0.99	1.00	1.00	1.00
80	0.97	0.97	0.98	0.98	0.99	0.99	0.99	1.00	1.00

(d)
T.C = 0.4

θ (°)	2	3	4	5	6	7	8	9	10
0	1.00	1.00	1.00	0.99	0.99	0.98	0.97	0.97	0.97
10	1.00	1.00	1.00	0.99	0.99	0.98	0.98	0.97	0.97
20	1.00	1.00	1.00	1.00	0.99	0.99	0.99	0.98	0.98
30	0.99	0.99	1.00	1.00	1.00	1.00	0.99	0.99	0.99
40	0.99	0.99	0.99	1.00	1.00	1.00	1.00	1.00	1.00
50	0.98	0.98	0.99	1.00	1.00	1.00	1.00	1.00	1.00
60	0.97	0.98	0.99	0.99	1.00	1.00	1.00	1.00	1.00
70	0.97	0.97	0.98	0.99	1.00	1.00	1.00	1.00	1.00
80	0.97	0.97	0.98	0.99	1.00	1.00	1.00	1.00	1.00

Figure 12. Displays heat map plots that illustrate the correlation between forecasted absorption measurements and the experimentally recorded values across various angles of incidence.

variable), the algorithm calculates residuals, trains a new weak learner to predict these residuals, and adds this learner to the ensemble with a weighted contribution determined by a learning rate parameter. This process continues for a specified number of iterations or until convergence, with the final prediction being the sum of all individual model predictions. Key hyperparameters include the number of estimators (boosting stages), learning rate (shrinkage factor), maximum depth of individual trees, and regularization parameters that help prevent overfitting [45–49].

Here, the dataset comprised 480 simulated samples derived from parametric FEM runs with the following features: incident angle (0°–80°), square ring size (4–10 µm), circular resonator radius (0.5–2.5 µm), and graphene chemical potential (0.1–0.9 eV). Each sample contained corresponding absorption and transmittance data. Data were randomly split (80:20) into training and test sets using seed = 42, and 5-fold cross-validation ensured statistical reliability. Gradient Boosting hyperparameters were optimized (n_estimators = 500, learning_rate = 0.05, max depth = 5, subsample = 0.9). Model evaluation yielded $R^2 = 0.97 \pm 0.02$, MAE = 0.008, and RMSE = 0.013, confirming high prediction accuracy.

The model's performance, illustrated in Figures 11–14, was evaluated using scatter plots and heat maps to assess predictive accuracy and parameter optimization. For incident angle variations (Figures 11 and 12), scatter plots showed a strong correlation with an optimal R^2 of 0.90, while heat maps achieved R^2 values between 0.97 and 1.00, indicating excellent model fit. Similarly, for the square ring geometry (Figures 13 and 14), scatter plots yielded an R^2 of 0.91, and heat maps showed R^2 values ranging from 0.94 to 1.00, confirming

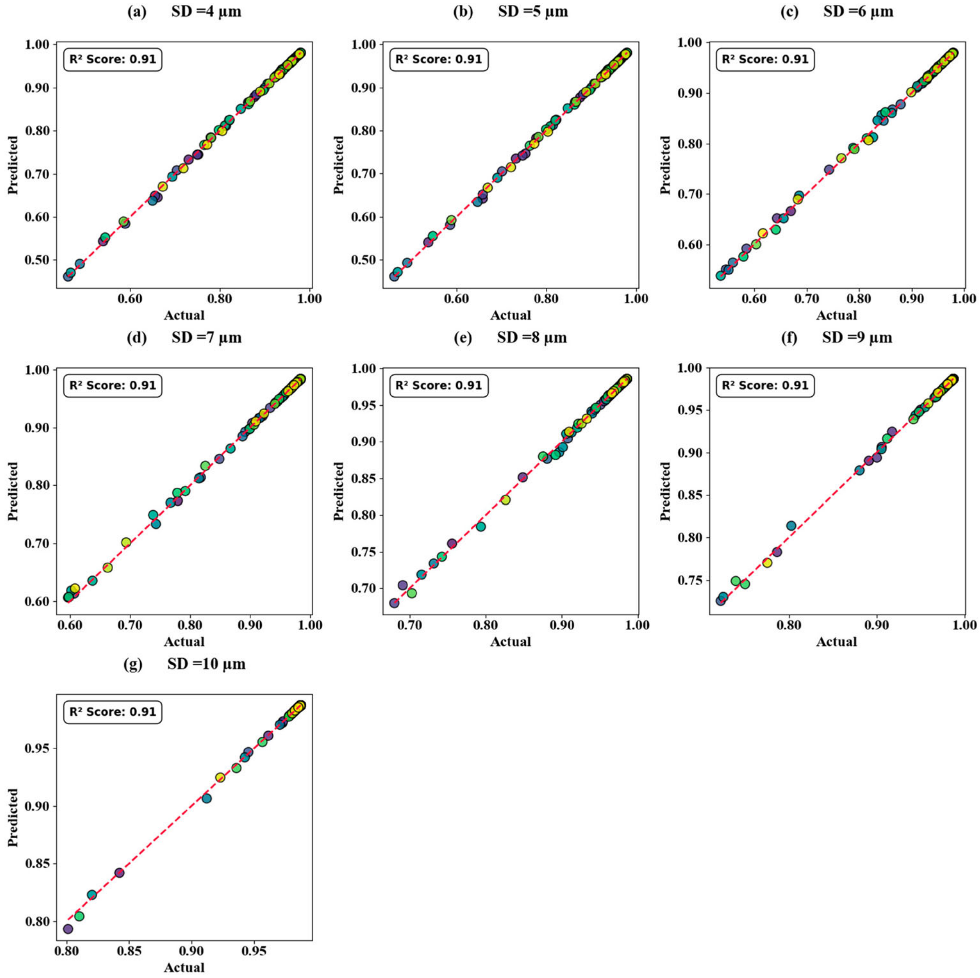

Figure 13. Displays scatterplot graphs that illustrate the correlation between forecasted absorption measurements and the experimentally recorded values across various square ring design parameters.

high predictive accuracy and robustness across different polynomial degrees and design parameters.

Conclusion

The proposed metasurface functions as a refractive index sensor capable of detecting dielectric perturbations caused by hCG presence. Despite hCG is considered here as a pregnancy-related biomarker, the same design can be extended to other biomolecules producing measurable RI shifts. Thus, the work demonstrates a generalizable plasmonic sensing platform for biomolecular and biochemical analytes. The sensor's unique architecture, featuring graphene-enhanced resonators with multi-metallic configurations, achieves unprecedented sensitivity levels of 1000 GHz/RIU and superior figure of merit values compared to existing biosensing platforms. The integration of terahertz frequency operation with localized surface plasmon resonance phenomena enables detection capabilities that

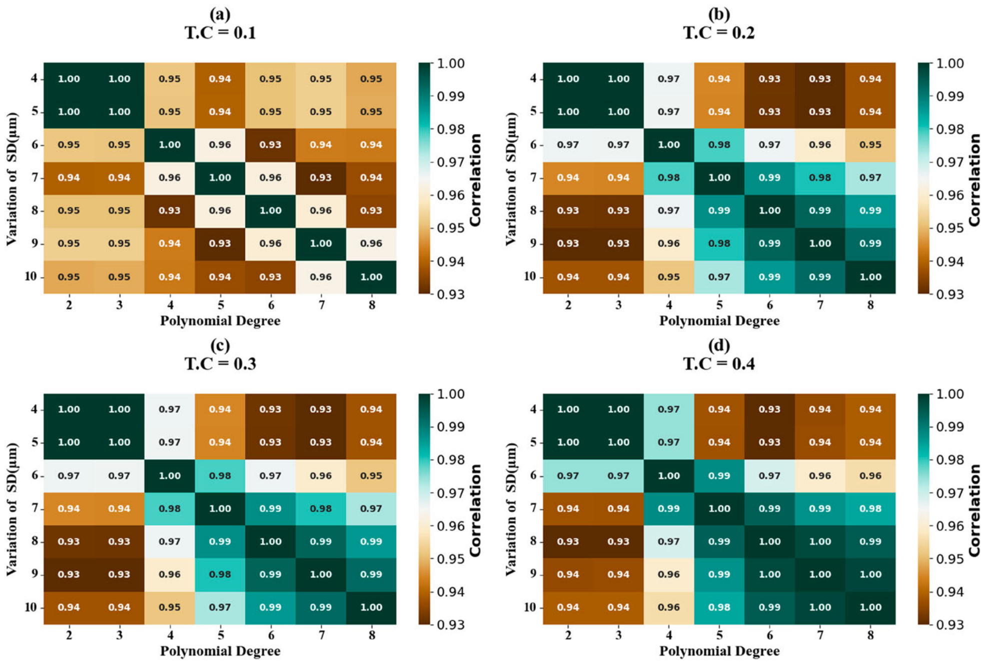

Figure 14. Displays heat map graphs that illustrate the correlation between forecasted absorption measurements and the experimentally recorded values across various Square ring design parameters.

significantly exceed conventional lateral flow assays, particularly for early-stage pregnancy detection and challenging cases such as ectopic pregnancies. The systematic optimization through electromagnetic modeling and machine learning algorithms ensures a robust performance across varying operational conditions, while the linear relationship between resonance frequency and refractive index changes ($R^2 = 0.88947$) provides a reliable calibration for quantitative hCG detection. Additionally, the successful implementation of Gradient Boosting Regressor machine learning models with R^2 scores reaching 1.00 across multiple design parameters validates the sensor's predictive accuracy and optimization potential. The comprehensive electromagnetic analysis reveals optimal operation at 0.3 THz with maximum field enhancement and absorption, confirming the theoretical predictions and design principles. Meanwhile, we believe that this work establishes a foundation for next-generation point-of-care diagnostic devices that combine advanced nanoplasmonics, metamaterial engineering, and artificial intelligence to deliver superior healthcare solutions. Future developments should focus on experimental validation, microfluidic integration for sample handling, and clinical trials to translate this promising technology into practical pregnancy testing devices that can bridge the healthcare gaps in resource-limited settings while providing enhanced accuracy and sensitivity for improved maternal and fetal health outcomes globally.

Acknowledgements

The authors acknowledge Princess Nourah bint Abdulrahman University Researchers Supporting Project number (PNURSP2025R5), Princess Nourah bint Abdulrahman University, Riyadh, Saudi Arabia

Disclosure statement

No potential conflict of interest was reported by the author(s).

Funding

This work was supported by the Princess Nourah bint Abdulrahman University (project number: PNURSP2025R5).

Availability of data and materials

The data supporting the findings in this work are available from the corresponding author with a reasonable request.

ORCID

Jonas Muheki https://orcid.org/0000-0001-6666-2785
William Ochen https://orcid.org/0009-0009-7639-7917

References

[1] Kennedy CE, Yeh PT, Gholbzouri K, et al. Self-testing for pregnancy: a systematic review and meta-analysis. BMJ Open. 2022;12(2):e054120. doi:10.1136/bmjopen-2021-054120
[2] Hashim NAF, Mahdy ZA, Abdul Rahman R, et al. Universal testing policy for COVID-19 in pregnancy: A systematic review. Front Public Health. 2022;10. doi:10.3389/fpubh.2022.588269
[3] Smits MAJ, van Maarle M, Hamer G, et al. Cytogenetic testing of pregnancy loss tissue: a meta-analysis. Reprod BioMed Online. 2020;40(6):867–879. doi:10.1016/j.rbmo.2020.02.001
[4] Gaudron E, Davis DL. Is carbon monoxide testing in pregnancy an acceptable and effective smoking cessation initiative? An integrative systematic review of evidence. Women Birth. 2024;37(1):118–127. doi:10.1016/j.wombi.2023.10.008
[5] D'Ippolito S, Longo G, Orteschi D, et al. Investigating the 'fetal side' in recurrent pregnancy loss: reliability of cell-free DNA testing in detecting chromosomal abnormalities of miscarriage tissue. J Clin Med. 2023;12(12). doi:10.3390/jcm12123898
[6] Morris N, Ehrenreich K, Gurazada T, et al. Feasibility and acceptability of at-home routine pregnancy testing in the United States: a pilot study. Women's Heal Issues. 2023;33(3):258–265. doi:10.1016/j.whi.2023.01.002
[7] Moon G, Lee J, Lee H, et al. Machine learning and its applications for plasmonics in biology. Cell Rep Phys Sci. 2022;3(9). doi:10.1016/j.xcrp.2022.101042
[8] Topor CV, Puiu M, Bala C. Strategies for surface design in surface plasmon resonance (SPR) sensing. Biosensors. 2023;13(4):465. doi:10.3390/bios13040465
[9] Das S, Devireddy R, Gartia MR. Surface plasmon resonance (SPR) sensor for cancer biomarker detection. Biosensors. 2023;13(3):396. doi:10.3390/bios13030396
[10] Bocková M, Slabý J, Špringer T, et al. Advances in surface plasmon resonance imaging and microscopy and their biological applications. Ann Rev Anal Chem. 2019;12:151–176. doi:10.1146/annurev-anchem-061318-115106
[11] Singh GP, Sardana N. Smartphone-based surface plasmon resonance sensors: a review. Plasmonics. 2022;17(5):1869–1888. doi:10.1007/s11468-022-01672-1
[12] Bilbao E, Garate O, Rodríguez Campos T, et al. Electrochemical sweat sensors. Chemosensors. 2023;11(4):244. doi:10.3390/chemosensors11040244
[13] He Q, Wang B, Liang J, et al. Research on the construction of portable electrochemical sensors for environmental compounds quality monitoring. Mater Today Adv. 2023;17:100340. doi:10.1016/j.mtadv.2022.100340
[14] Li Y, Luo L, Kong Y, et al. Recent advances in molecularly imprinted polymer-based electrochemical sensors. Biosens Bioelectron. 2024;249:116018. doi:10.1016/j.bios.2024.116018

[15] Rajakannu A, Wekalao J, Elsayed HA, et al. A high sensitivity terahertz biosensor with hybrid metasurfaces for tuberculosis detection leveraging the integration of machine learning and multi – material resonators. Brazilian J Phys. 2025;55(4). doi:10.1007/s13538-025-01811-z
[16] Anbazhagan S, Arun Kumar U, Rajakannu A, et al. AI-augmented terahertz biosensor with MXene – graphene architecture for sensitive sperm concentration detection. Plasmonics. 2025;20(11):10573–10587. doi:10.1007/S11468-025-03154-6
[17] Shah A, Ur S, Irshad R. Fdtd simulations of plasmon propagation in the transient plasma corona due to ionization attachment and recombination processes. Plasmonics. 2025;123456789. doi:10.1007/s11468-025-03255-2
[18] Xu L, Liu W, Luo X, et al. High-Sensitivity D-type Six-hole PCF-SPR sensor. Plasmonics. 2025;20(6):4149–4157. doi:10.1007/s11468-024-02530-y
[19] Fei Y, Luo B, An M, et al. Highly sensitive surface plasmon resonance refractive index sensor based on D-shaped dual–core photonic crystal fiber with ITO film. Plasmonics. 2024;19(3):1633–1647. doi:10.1007/s11468-023-02103-5
[20] Vinoth R, Thangavel G, Wekalao J, et al. Ultra-High sensitivity terahertz detection using a 2D-material-based metasurface: design, tuning, and machine learning validation. Plasmonics. 2025;20(8):6139–6150. doi:10.1007/s11468-025-03118-w
[21] Aggarwal K, Wekalao J, Rajakannu A. A trimodal 2D metasurface biosensor with Bayesian regression for ultra – sensitive cancer biomarker detection. Plasmonics. 2025;20(8):5977–5990. doi:10.1007/s11468-025-03033-0
[22] Maier SA. Plasmonics: fundamentals and applications. Berlin: Springer; 2007. doi:10.1007/0-387-37825-1_2
[23] Maier SA, Fundamentals and applications plasmonics: fundamentals and applications, vol. 677, no. 1. 2004.
[24] Boulais E, Lachaine R, Hatef A, et al. Plasmonics for pulsed-laser cell nanosurgery: fundamentals and applications. J Photochem Photobiol C: Photochem Rev. 2013;17:26–49. doi:10.1016/j.jphotochemrev.2013.06.001
[25] Low T, Avouris P. Graphene plasmonics for terahertz to mid-infrared applications. ACS Nano. 2014;8(2):1086–1101. doi:10.1021/nn406627u
[26] Jablan M, Buljan H, Soljačić M. Plasmonics in graphene at infrared frequencies. Phys Rev B Condens Matter Mater Phys. 2009;80(24). doi:10.1103/PhysRevB.80.245435
[27] Yuksel M, Luo W, McCloy B, et al. A precise and rapid early pregnancy test: development of a novel and fully automated electrochemical point-of-care biosensor for human urine samples. Talanta. 2023;254:124156. doi:10.1016/j.talanta.2022.124156
[28] Bocková M, Chadtová Song X, Gedeonová E, et al. Surface plasmon resonance biosensor for detection of pregnancy associated plasma protein A2 in clinical samples. Anal Bioanal Chem. 2016;408(26):7265–7269. doi:10.1007/s00216-016-9664-z
[29] Patel SK, Surve J, Parmar J, et al. Recent advances in biosensors for detection of COVID-19 and other viruses. IEEE Rev Biomed Eng. 2023;16:22–37. doi:10.1109/RBME.2022.3212038
[30] Patel SK, Surve J, Parmar J, et al. Graphene-based H-shaped biosensor with high sensitivity and optimization using ML-based algorithm. Alexandria Eng J. Apr 2023;68:15–28. doi:10.1016/j.aej.2023.01.002
[31] Patel SK, Surve J, Katkar V, et al. Encoding and tuning of THz metasurface-based refractive index sensor with behavior prediction using XGBoost regressor. IEEE Access. 2022;10:24797–24814. doi:10.1109/ACCESS.2022.3154386
[32] Jadeja R, Surve J, Parmar T, et al. Detection of peptides employing a THz metasurface based sensor. Diam Relat Mater. Jan 2023;132:109675. doi:10.1016/j.diamond.2022.109675
[33] Wekalao J. High-Sensitivity glucose detection using a terahertz metasurface-based surface plasmon resonance biosensor with graphene and plasmonic nanostructures, optimized by machine learning. Plasmonics. 2025: 123456789. doi:10.1007/s11468-025-02815-w
[34] Vaijayanthimala J, Vaishnavi K, Arun Kumar U, et al. High-Sensitivity terahertz metasensor for cervical cancer diagnosis: graphene modulation and XGBoost-assisted optimization. Sensors Int. 2025;7:100350. https://www.sciencedirect.com/science/article/pii/S2666351125000257

[35] Almawgani AHM, Wekalao J, U AK, et al. Design and optimization of encoded and tunable graphene-silver metasurface surface plasmon resonance sensor for detection of Low refractive index variation in terahertz regime. Plasmonics. 2025;20(7):4439–4449. doi:10.1007/s11468-024-02613-w

[36] Nagarajan P, Gupta SK, Oruganti SK, et al. Advanced FET-compatible graphene-silver-gold multilayered high-sensitivity biosensor for rapid COVID-19 detection with behavior prediction. Plasmonics. 2025;20(8):6289–6302. doi:10.1007/S11468-025-03197-9

[37] Alsaif H, Wekalao J, Ali NB, et al. Design and optimization of a MXene-based terahertz surface plasmon resonance sensor for malaria detection. Plasmonics. 2025;20(4):2153–2163. doi:10.1007/s11468-024-02455-6

[38] Selvi RS, Murugesan RR, Wekalao J, et al. Advanced MXene-gold hybrid plasmonic biosensor for early detection of tuberculosis biomarkers With machine learning optimization. Plasmonics. 2025. doi:10.1007/s11468-025-03178-y

[39] Wekalao J, Patel SK, Anushkannan NK, et al. Design of ring and cross shaped graphene metasurface sensor for efficient detection of malaria and 2 bit encoding applications. Diam Relat Mater. 2023;139(August):110401. doi:10.1016/j.diamond.2023.110401

[40] Kumar R, Rai B, Samui P. A comparative study of prediction of compressive strength of ultra-high performance concrete using soft computing technique. Struct Concr. 2023;24(4):5538–5555. doi:10.1002/suco.202200850

[41] Panda SK, Mohanty SN. Time series forecasting and modeling of food demand supply chain based on regressors analysis. IEEE Access. 2023;11:42679–42700. doi:10.1109/ACCESS.2023.3266275

[42] Nyirandayisabye R, Li H, Dong Q, et al. Automatic pavement damage predictions using various machine learning algorithms: evaluation and comparison. Results Eng. 2022;16. doi:10.1016/j.rineng.2022.100657

[43] Rathakrishnan V, Bt. Beddu S, Ahmed AN. Predicting compressive strength of high-performance concrete with high volume ground granulated blast-furnace slag replacement using boosting machine learning algorithms. Sci Rep. 2022;12(1):63. doi:10.1038/s41598-022-12890-2

[44] Bijlwan A, Pokhariyal S, Ranjan R, et al. Machine learning methods for estimating reference evapotranspiration. J Agrometeorol. 2024;26(1):63–68. doi:10.54386/jam.v26i1.2462

[45] Merdas HM, Mousa AH. Food sales prediction model using machine learning techniques. Int J Electr Comput Eng. 2023;13(6):6578–6585. doi:10.11591/ijece.v13i6.pp6578-6585

[46] Godasiaei SH, Chamkha AJ. Exploring novel heat transfer correlations: machine learning insights for molten salt heat exchangers. Numer Heat Transf Part A Appl. 2025;86(14):5047–5064. doi:10.1080/10407782.2024.2321524

[47] Omar I, Khan M, Starr A. Comparative analysis of machine learning models for predicting crack propagation under coupled load and temperature. Appl Sci. 2023;13(12):7212. doi:10.3390/app13127212

[48] Prakash MC, Saravanan P. Crop insurance premium recommendation system using artificial intelligence techniques. Int J Prof Bus Rev. 2023;8(4):e01270. doi:10.26668/businessreview/2023.v8i4.1270

[49] Anjum M, Khan K, Ahmad W, et al. Application of ensemble machine learning methods to estimate the compressive strength of fiber-reinforced nano-silica modified concrete. Polymers (Basel). 2022;14(18):3906. doi:10.3390/polym14183906